Research Article | Vol. 31, No. 8 / 10 Apr 2023 / Optics Express 12894

Optics EXPRESS

Continuous fabrication of polarization maintaining fibers via an annealing improved infinity additive manufacturing technique for THz communications

GUOFU XU AND MAKSIM SKOROBOGATIY*

Department of Engineering Physics, École Polytechnique de Montréal, Montreal, Québec, H3T 1J4, Canada

*maksim.skorobogatiy@polymtl.ca

Abstract: We report the design and fabrication of a polarization-maintaining fiber for applications in fiber-assisted THz communications. The fiber features a subwavelength square core suspended in the middle of a hexagonal over-cladding tube by four bridges. The fiber is designed to have low transmission losses, high birefringence, high flexibility, and near-zero dispersion at the carrier frequency of 128 GHz. An infinity 3D printing technique is used to continuously fabricate a 5 m-long polypropylene fiber of ~6.8 mm diameter. The fiber transmission losses are furthermore reduced by as high as ~4.4 dB/m via post-fabrication annealing. Cutback measurements using 3 m-long annealed fibers show ~6.5-11 dB/m and ~6.9-13.5 dB/m losses (by power) over a 110-150 GHz window for the two orthogonally polarized modes. Signal transmission with bit error rates of $\sim 10^{-11}$-10^{-5} is achieved at 128 GHz for 1-6 Gbps data rates using a 1.6 m-long fiber link. The average polarization crosstalk values of ~14.5 dB and ~12.7 dB are demonstrated for the two orthogonal polarizations in fiber lengths of 1.6-2 m, which confirms the polarization-maintaining property of the fiber at ~1-2 meter lengths. Finally, THz imaging of the fiber near-field is performed and shows strong modal confinement of the two orthogonal modes in the suspended-core region well inside of the hexagonal over-cladding. We believe that this work shows a strong potential of the infinity 3D printing technique augmented with post-fabrication annealing to continuously produce high-performance fibers of complex geometries for demanding THz communications applications.

1. Introduction

In the past two decades, the terahertz (THz) spectral range (0.1 THz-10 THz) positioned between microwave and infrared spectral ranges has been a research hotspot with potential applications in many fields, such as imaging [1–4], sensing [5–8], security [9–11], communications [12–14], and biomedicine [15–19]. THz communications, in particular, have attracted strong attention due to the unique properties of THz waves that offer higher bandwidths and higher directivities compared to microwaves. Moreover, THz waves feature lower scattering losses, and higher diffuse reflection losses and are safer than infrared waves [20–22]. To date, THz wireless communications have experienced the most rapid development due to the convenience of wireless links between the end-users and base stations. At the same time, successful deployment of THz wireless systems requires solutions to many technical challenges including high atmospheric absorption under severe weather conditions [23–25], high free space path loss due to self-diffraction [26], tight alignment tolerance between the transmitting and receiving antennas [27–29], security against eavesdropping [30–32], etc. To mitigate these challenges, THz fibers and fiber-based components can aid in building high-fidelity THz communication systems due to their advantages of flexibility, small footprint, high integrability, ease of handling, and immunity to external perturbations when properly encapsulated. To date, a variety of THz fibers have been designed, fabricated, and tested

#486400 https://doi.org/10.1364/OE.486400
Journal © 2023 Received 26 Jan 2023; revised 6 Mar 2023; accepted 16 Mar 2023; published 3 Apr 2023

in THz communication links, including photonic crystal waveguides [33–35], topological valley photonic crystal waveguides [36], effective-medium-added dielectric waveguides [37], dielectric waveguides with rectangular or square cross-sections [38–44], metal waveguide [45], dielectric and metalized hollow-core fibers [46–49], subwavelength rod-in-air fibers [50–53], suspended core fibers [54,55], porous fibers [56], etc. Moreover, various functional fiber/waveguide-based devices have been realized for signal processing in THz communication applications, such as dielectric fiber/waveguide-based couplers and multiplexers [57–60], two-wire waveguide-based splitters, and multiplexers [61–63], metalized hollow-core waveguide-based dispersion compensators [64], etc. The above-mentioned developments in fiber-assisted THz communications were recently reviewed in Ref. [65], which reveals strong prospects for fiber/waveguide-assisted devices in the field of THz communications.

To increase the THz fiber link length and to boost the data rates supported by the fiber links one has to reduce the link transmission losses, which is often achieved by compelling a large fraction of the modal fields to propagate in the low-loss air region of the fiber. Another important feature of the THz fiber design is judicial dispersion management, including operation near zero dispersion wavelength, adopting dispersion flattened fiber designs [66,67], or utilizing pre/post-dispersion compensation [64]. Moreover, by employing multiplexing techniques, such as frequency/polarization-division multiplexing, multi-channel communications over broader bandwidth are achievable. Recently, several devices using frequency-division multiplexing have been demonstrated for THz communications, such as the four-port THz add-drop multiplexers based on two-wire plasmonic waveguides [63], as well as the silicon-based frequency differentiation coupler and multiplexers [59,60]. In addition, a silicon-in-air waveguide with a square cross-section [39] and a four-wire waveguide with a square arrangement [62] have been proposed for polarization-division multiplexing.

To date, most of the emitters, receivers, and signal processing devices in the THz range are polarization sensitive. When propagating along the non-polarization maintaining fiber, THz waves could change their state of polarization, thus making the reliable signal detection at the receiver end problematic. For example, during operation the fiber might be subjected to changing environmental conditions (temperature, pressure, etc.), as well as direct mechanical action (bending, stretching, etc.), thus resulting in a change in the THz wave polarization state at the fiber output end. Therefore, there is currently a strong need for polarization-maintaining fibers (PMF) in the THz spectral range capable of maintaining a predictable polarization state of the guided modes. PMFs can be designed by introducing high modal birefringence through asymmetric core and cladding structures. Modal birefringence is defined as the difference in the effective refractive index between two orthogonal linear-polarization modes [68]. Additionally, the ability of such fibers to maintain a given polarization state can be quantitatively expressed using polarization crosstalk defined as the ratio of the output power in the input polarization to that in the orthogonal polarization [68,69] at the end of the fiber link.

Various designs of polarization-maintaining waveguides and fibers for the THz range have been proposed. Photonic crystal fibers (PCFs), in particular, have received significant attention for realizing PMFs due to the high tunability of their structure. Among many designs of the PCF-assisted PMFs, we note fibers featuring asymmetric porous cores [70–81], suspended asymmetric porous cores [82,83], inclination-optimized asymmetric cores [84,85], asymmetric air cores [86–89], and anisotropic porous/solid cores [90–94]. Such PMFs were designed for 0.1-5 THz, and they feature relatively high birefringence of $\sim 10^{-3}$-10^{-1}. Moreover, porous THz fibers with asymmetric features have also been used to achieve high birefringence ($\sim 10^{-3}$-10^{-2} in ~0.3-2 THz) by employing slotted rectangular pores [95], lattice elliptical pores [96,97], and asymmetric distribution of pore lattices [98]. Unfortunately, both PCFs and porous fibers feature high porosities and require precise control over the shapes of the air inclusions, which poses significant challenges for fiber fabrication, thus limiting most studies to the theoretical domain (only Ref. [94] was experimentally realized).

A simpler way to implement PMFs is using polymer elliptical tubes (ARROW waveguides) which have been demonstrated to achieve high birefringence of ~10^{-2} (~0.8-2 THz) [99–101]. Although such PMFs have a simple structure, the poor mechanical strength makes them susceptible to deformation, thus limiting the practical applications of such fibers. Furthermore, several hollow-core anti-resonant THz fibers [102–105] have been theoretically proposed to achieve a moderate birefringence of ~10^{-5}-10^{-4} in the frequency range of ~0.5-2 THz. The birefringence of hollow-core fibers can be greatly increased to ~10^{-3}-10^{-2} (~0.2-1.5 THz) by using an elliptical hollow-core [106] or metalized elliptical hollow core [107]. However, to ensure low-loss propagation, the size of the hollow core has to be relatively large, which makes such fibers large, inflexible, and inconvenient to deploy.

In contrast to hollow-core fibers, solid-core fibers typically feature higher flexibility and smaller dimensions, and they are much easier to fabricate. Solid core fibers have been theoretically shown to achieve a birefringence of ~10^{-3}-10^{-2} in the range of 0.5-1 THz by using rectangular/elliptical rod-in-air designs [108]. As the optical performance of rod-in-air fibers is susceptible to environmental variations, encapsulated suspended core fibers were proposed to address this problem. Thus, solid core fibers with birefringence of ~10^{-2} over 0.6-1.4 THz were reported in [109,110] for applications in polarization filtering.

Among the above-mentioned PMFs, only three have been experimentally realized with lengths of ~0.02-0.29 cm and birefringence in the range of ~10^{-3}-10^{-2}[94,106,107], while two of the three PMFs are quite lossy (~tens to hundreds dB/m) [94,106]. The other one has been demonstrated to have a transmission loss smaller than ~2 dB/m at 0.65 THz by utilizing a silver-coated elliptical hollow core fiber [107], however, this design also makes it less cost-effective and less resistant to bending. Moreover, to date, the majority of work on polarization-maintaining fibers in the THz spectral range mostly concentrates on achieving high modal birefringence, while dispersion management is often missing from the fiber design. Given the relatively high dispersions of unoptimized solid core THz fibers, the transmission data rates of even short several-meter-long THz fiber communication links can be severely limited without proper dispersion management.

In this work, we report the design, fabrication, and optical characterization of a suspended subwavelength core polarization maintaining THz fiber that features high birefringence, small size, relatively high flexibility, relatively low transmission loss, and optimized dispersion characteristics for applications in fiber-assisted THz communications. The fiber features a square subwavelength core suspended in the air by four thin bridges in the middle of a hexagonal encapsulation tube that serves to isolate the fiber core mode from the environment. The dimensions (width and length) and inclinations of the four bridges were optimized to result in high birefringence of the two fundamental guided modes. Moreover, the group velocity dispersions (GVD) of the two PMF modes were minimized to support high communication bit rates at the carrier frequency of 128 GHz. Then, owing to the recent development of additive manufacturing technique [111], a novel infinity 3D printing technique was used to continuously fabricate the proposed fiber without limitation in the fiber length and without the need for any supporting structure. Finally, we demonstrate that the transmission loss of the infinity 3D printed fibers could be significantly reduced via post-fabrication annealing. As summarized in Table 1, compared to other fused deposition modeling (FDM) printed fibers reported in the literature [5,54,112–116], our infinity printed fiber features a smaller diameter (thus higher flexibility), longer lengths, and relatively low transmission loss, which highlights the strong potential of this technique for the fabrication of THz fibers of complex transverse geometries.

The paper is organized as follows: In Section 2, we first introduce the design and optimization strategy of the PMF followed by the details of the fiber fabrication process. Section 3 presents the theoretical analysis of the optical properties of the two orthogonally polarized fundamental

Optics EXPRESS

Table 1. Comparison of FDM-based 3D Printed THz Fibers

Fiber Structure	Diameter (mm)	Length (cm)	Loss (dB/m)	Frequency (THz)	Ref.
Hollow core	~36.5	~5-12.5	~100-500	0.18-0.32	[5]
Hollow core	~25	~10	~30-150	0.1-0.4	[112]
Hollow core	~24	~8.7	~102-104	0.15-0.5	[113]
Hollow core	~23	~9.3	~60-160	0.1-0.3	[114]
Hollow core	~45	~90	~13	0.1	[115]
Hollow core	~12	~2-5	~40-500	0.35-0.9	[116]
Suspended core	~8	~140-250	~3-24	0.11-0.15	[54]
Suspended core	~6.8	~300	~6-14	0.11-0.15	This work

modes of the PMF, including their absorption losses in straight fibers, radiation losses in bent fibers, modal excitation efficiencies, group velocity dispersion, and projected bit rate capacities of the PMF links. Section 4 presents the experimental characterization of the PMF before and after annealing, which includes transmission losses, polarization crosstalk, data communication performance, and near-field modal imaging.

2. Fiber design and fabrication with infinity 3D printer

The schematic of the proposed PMF fiber cross-section is shown in Fig. 1(a), where the blue and white regions represent the polypropylene (PP) material and air respectively. The fiber structure is optimized to feature near-zero dispersion for the X-polarized fundamental mode at the optimal carrier frequency (128 GHz) of our THz communication system [50]. At the same time, the design aims at achieving high modal birefringence, and small fiber size, while minimizing leakage loss from the core to the cladding encapsulation tube (see Supplement 1 Sec. S1 for details of the optimization process). An optimized fiber features a square solid core of size d_c=1.6 mm, suspended by four bridges of width W_b=0.5 mm. The inclination angle of the four bridges with respect to the Y-axis is $\theta_b = 8°$. The size of the hexagonal cladding tube is $D_t = 6.8$ mm, and its thickness is $W_t = 0.4$ mm.

Thus optimized fiber was fabricated using the infinity fused deposition modeling (IFDM) 3D printing technique using polypropylene polymer that features one of the lowest losses in the THz range. Within the IFDM technique, the fiber is continuously printed on a sliding belt using an inclined extrusion nozzle [Fig. 1(b)], thus allowing the printing of unlimited in-length waveguides of the arbitrarily complex geometric cross-sections. In this work, we used a Powerbelt3D Zero IFDM that features a 35° inclined extrusion nozzle of 0.2 mm diameter. The printing parameters, including infill flow rate, infill speed, layer height, etc. were first optimized by minimizing the amount of air trapped in solid bulk regions following the methodology described in ref. [54]. After a comprehensive printing parameter optimization, the optimal settings for the IFDM and polypropylene used in this work were found to be: infill flowrate of 150%, layer height of 0.16 mm, infill speed of 25 mm/s, outer(inner) shell speeds of 25(5) mm/s, the overlap of 10% and extrusion temperature of 240 °C. Then, a 5 m-long fiber was fabricated after a total of ~50 hours of uninterrupted printing. To enhance the stability of the printing process, the fiber was chosen to lay flat on the belt on one of the sides of its hexagonal cladding.

The microscopy image of the printed fiber cross-section and the photo of a coiled 5 m-long fiber are shown in Figs. 1(c) and 1(d). The resultant fiber features a suspended trapezoidal core of sizes that vary in the ~1.45-1.65 mm range. The widths of the four bridges are ~0.45-0.55 mm, the thickness of the cladding shell is ~0.4-0.5 mm, and the fiber size is ~6.8 mm. The uniformity of the fabricated fiber was verified during the cut-back measurements by dissecting a ~3 m fiber section every ~25 cm while observing almost identical cross-sections. The surface roughness of

Optics EXPRESS

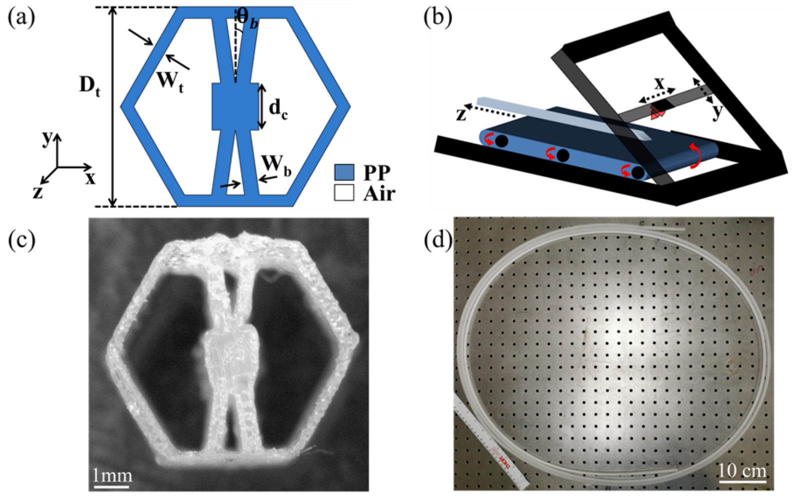

Fig. 1. (a) Schematic of the PMF cross-section. (b) Schematic of the PMF fabrication process with an infinity 3D printer. (c) Microscopy image of the fabricated PMF cross-section, as well as (d) the side view of the infinity-printed continuous 5 m-long PMF.

the fiber core walls along the fiber direction is estimated to be ~35 µm (see Supplement 1 Sec. S3). The sizes of the features in the fiber cross-section deviate somewhat from the design by ~50-100 µm, which we attribute to the printer resolution.

3. Theoretical analysis of the polarization-maintaining fiber

In this section, we study theoretically the key optical properties of the optimized polarization-maintaining fiber, including their modal loss, excitation efficiency, bending loss, and group velocity dispersion that directly impact the maximal transmission length and bit rate of the communication links.

3.1. Modal structure of the straight PMF

The theoretical studies were conducted using the finite element COMSOL Multiphysics software and the ideal cross-section of the PMF shown in Fig. 1(a). The outer cladding of the fiber was lossless air with n_{air}= 1, while the effective refractive index n_{PP} and absorption coefficient α_{PP} (by power) of the printed Polypropylene were taken as n_{PP}= 1.485 and α_{PP} $[dB/m]$ = $236.31\ \nu^2 - 37.75\ \nu + 3.32$ in the frequency range of (0.11-0.15 THz) as found in our prior experimental study [50].

The normalized electric field distributions and electric field directions (red arrows) of the two orthogonally polarized (X-pol and Y-pol) fundamental modes of the optimized PMF are presented in Fig. 2(a) in the frequency range of 110-150 GHz. In the numerical simulations, the half computational cell and the perfect electric conductor (PEC) boundary condition along the symmetry plane [ZOY defined in Fig. 1(a)] was used for calculating the X-polarized mode, while the perfect magnetic conductor (PMC) boundary was used for the Y-polarized mode.

In Fig. 2(b), we present the effective refractive indexes of the two modes that show monotonic increases at higher frequencies. This is due to the stronger confinement of the modal fields in the fiber core at higher frequencies, which is seen from the normalized electric field distributions in Fig. 2(a). Furthermore, the Y-polarized mode shows higher effective refractive indices than the X-polarized mode due to the presence of the bridges in the Y direction, thus effectively leading to a larger core size in this direction. At the same time, both modes have effective refractive indices

Optics EXPRESS

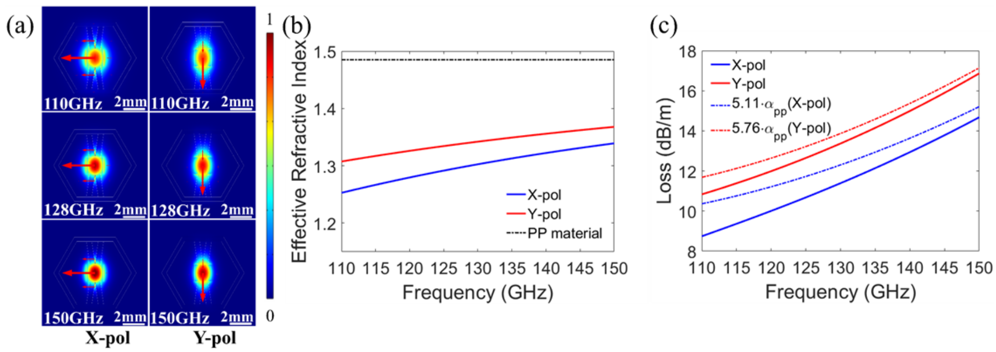

Fig. 2. (a) Normalized electric field distributions and electric field directions (red arrows) of the two orthogonally polarized fundamental modes for the PMF at various frequencies. (b) Theoretical effective refractive indexes and (c) transmission losses (by power) of the two orthogonally polarized fundamental modes for the PMF as a function of frequency. The dotted lines show corresponding effective material losses.

that are much smaller than that of the bulk polypropylene, thus signifying that a large part of their modal fields propagates in the lossless air cladding. The computed modal birefringence is high, and it is ~0.03-0.05 in the 110-150 GHz range.

We now discuss the modal transmission losses of the PMF. These comprise the material absorption losses of the printed Polypropylene, the radiation scattering losses on the imperfect fiber interfaces (e.g., core roughness due to the printing process), as well as radiation loss due to modal leakage from the core through the bridges and into the fiber cladding. A proper simulation of each of those loss mechanisms is a complicated task, which requires detailed knowledge of the statistical distributions of the geometric and material imperfections, and as such deserves a separate study beyond the scope of this work. Instead, to match the numerical losses of the PMF modes to the experimental ones we use a much simpler, albeit less physically motivated concept of the effective material loss. In such a model one lumps all the loss mechanisms into an effective material absorption loss, which is then found separately for each polarization by fitting the numerical data to the experimentally measured one [49]. One way of parametrizing an effective material loss is by assuming that it is simply proportional to the Polypropylene bulk material loss α_{PP} up to a multiplicative factor (that is larger than 1). Such a factor is then found to best reproduce the experimentally measured transmission losses. If the multiplicative factor is close to 1, it means that bulk material losses dominate transmission losses. On the other hand, if a multiplicative factor is much larger than one, it would mean that other sources of loss beyond material absorption dominate.

For the case of a PMF considered in this work, we find that experimental transmission losses of the two orthogonally polarized modes are best reproduced numerically by assuming the effective material losses of ~5.11·α_{PP} for the X-polarized mode, and ~5.76·α_{PP} for the Y-polarized mode. The multiplicative factors were calculated using the least-squares method for minimizing the fitting error between the theoretical and experimental losses (shown in Fig. 5). As seen in Fig. 2(c), the transmission loss of the Y-polarized mode is somewhat higher than that of the X-polarized mode. This is because the Y-polarized mode has a larger modal field presence in the transitional region between the core and the bridges [see Fig. 2(a)] which shows a high degree of geometrical imperfections in the printed structure. The transmission losses of the X-polarized and Y-polarized modes are estimated to be ~8.7-14.7 dB/m and ~10.8-16.9 dB/m in the range of 110-150 GHz, with the corresponding losses of ~11.1 dB/m and ~13.1 dB/m at the carrier frequency of 128 GHz.

Optics EXPRESS

Furthermore, the numerical simulations of the bent PMF in two orthogonal fiber bending directions reveal that the PMF can readily tolerate tight bends with radii as small as ~2 cm at the carrier frequency of 128 GHz, resulting in only a small loss increase of less than 0.01 dB per 90° bend for both polarizations (see Supplement 1 Sec. S2 for the modal properties of the bent PMF).

3.2. Excitation efficiencies of the two orthogonally polarized modes

Next, the excitation efficiencies of the two orthogonally polarized modes excited with a WR-6 waveguide flange are studied. The flange supports a single linearly polarized mode with transverse electric field direction along the shorter side of a rectangular metallic waveguide [see panels III and IV in Fig. 3(c)]. The complex modal excitation coefficient can be computed using the following expression [117]:

$$C_m = \frac{\iint (E^*_{mode} \times H_{wg} + E_{wg} \times H^*_{mode}) dxdy}{\sqrt{\iint 2Re(E^*_{wg} \times H_{wg}) dxdy}\sqrt{\iint 2Re(E^*_{mode} \times H_{mode}) dxdy}} \tag{1}$$

where E_{wg} and H_{wg} are the transverse electric and magnetic fields of the WR-6 rectangular metallic waveguide, while E_{mode} and H_{mode} are the transverse electric and magnetic fields of a given fiber mode. Then, the relative power of the fiber modes excited with the WR-6 waveguide mode is given by $|C_m|^2$ which we refer to as excitation efficiency in the rest of the paper. It should be noted that expression (1) is derived assuming lossless waveguides/fibers. However, even in the case of lossy waveguides, expression (1) is an excellent approximation to coupling efficiency as long as the imaginary part of the modal propagation constant is much smaller than the real one, which holds for the fiber modes in our study.

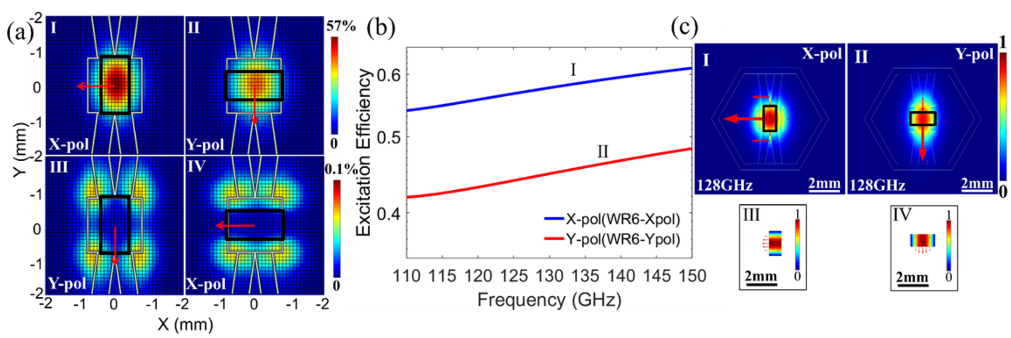

Fig. 3. (a) Excitation efficiencies of the X-polarized (panel I) and Y-polarized (panel II) modes as a function of the center position of the WR-6 waveguide at 128 GHz. The white solid lines, black rectangles, and red arrows represent fiber boundaries, optimized (both the orientation and position) WR-6 waveguide, and the electric field directions of the two fiber modes, respectively. Panels III and IV show maps of parasitic coupling to the other polarization due to spatial misalignment from the optimal coupling arrangement. (b) Excitation efficiencies of the X-polarized and Y-polarized modes versus frequency for the optimal coupling arrangement. (c) Normalized electric field distributions and electric field directions (red arrows) of the two fiber modes (I and II) and the WR-6 waveguide mode (III and IV) at 128 GHz. Black rectangles show the orientations and positions of the WR-6 waveguide presented in panels III and IV.

To maximize the excitation efficiencies of the X-polarized and Y-polarized modes, one has to optimize both the relative electric field direction and position between the fiber and WR-6 waveguide modes. In our experiment, both the orientation and position of the WR-6 waveguide flange are optimized relative to the fixed PMF. Therefore, in the simulations, the excitation

Optics EXPRESS

efficiencies of the X-polarized and Y-polarized modes are firstly optimized by aligning the modal polarization of the WR-6 waveguide mode with the principal polarization directions of the two orthogonally polarized modes, which are theoretically and experimentally found to be the directions along X and Y axes as defined in Fig. 1(a). Then, by scanning the fiber profile with a WR-6 waveguide, the relative position between the fiber and WR-6 waveguide maximizes excitation efficiency can be identified. As a result, the maps of excitation efficiencies for the X-polarized and Y-polarized modes versus the center position of the WR-6 waveguide operating at 128 GHz are presented in Fig. 3(a) panels I and II, in which the orientation of the WR-6 waveguide is also optimized with respect to a fixed PMF represented by the white solid lines. The maximum excitation efficiencies of ~57% and ~44% can be obtained for the X-polarized and Y-polarized modes at 128 GHz, respectively. Subsequently, the excitation efficiencies of the two modes over the frequency range of 110-150 GHz with the WR-6 optimized for either X-polarized or Y-polarized mode are shown in Fig. 3(b). The excitation efficiencies range between ~54%-61% and ~42%-48% for X-polarized and Y-polarized modes when the electric field direction of the WR-6 waveguide is correctly aligned with that of the two fundamental PMF modes [see I and II in Figs. 3(b) and 3(c)]. Note also that from the symmetry considerations it follows that for the optimal coupling conditions for the X or Y polarized modes [see panels I and II in Fig. 3(a)], parasitic coupling to the other polarizations is exactly zero. Alternatively, in case of misalignment from the optimal coupling arrangement, the parasitic coupling is indeed possible but it stays very small (below 0.1%) even for spatial deflections from the optimal position as large as ~1 mm [see panels III and IV in Fig. 3(a)].

3.3. Modal group velocity dispersion and maximum bit rates

Dispersion management is an important issue for THz fiber links and is commonly employed to reduce signal distortion and increase data transmission rates. One approach is to employ a dispersion compensator to negate the effect of the total dispersion incurred over the whole transmission link [64], while another alternative is to directly reduce the GVD of the transmission link by properly optimizing the fiber geometry [54,66], which is also the strategy used in this work. GVD of a fiber mode in the vicinity of a carrier angular frequency ω_0 can be inferred from the Taylor expansion of the modal dispersion $\beta(\omega)$ as follows:

$$\beta(\omega) = \beta(\omega_0) + \beta'(\omega_0)(\omega - \omega_0) + \frac{1}{2}\beta''(\omega_0)(\omega - \omega_0)^2 + \cdot\cdot\cdot, \qquad (2)$$

where modal dispersion is defined as the second-order derivative of the modal propagation constant $\beta''(\omega_0)$ [118].

The dispersion of the X-polarized and Y-polarized modes as a function of frequency are presented in Fig. 4(a) for our optimized dispersion-managed fiber. In fact, the fiber geometrical parameters were chosen to result in the X-polarized mode featuring a zero dispersion at the carrier frequency of 128 GHz. For the Y-polarized mode, the dispersion varies between ~-1-4 ps/THz/cm in the frequency range of 110-150 GHz, with the near-zero dispersion frequency shifted to ~140 GHz. Then the maximum bit rate support by the two modes for the link length of L=2 m is estimated with the following expression [119]:

$$BR_{max} = 1/\left(4\sqrt{|\beta''(\omega_0)|L}\right) \qquad (3)$$

Moreover, the upper limit of the maximum error-free bit rate near zero dispersion frequency is estimated using the third-order modal dispersion [119]:

$$BR_{ZD} = 0.324/\sqrt[3]{|\beta'''(\omega_0)|L} \qquad (4)$$

where β''' is the third-order derivative of the modal propagation constant. The frequency-dependent maximum bit rates BR_{max} supported by the two modes for the link length of 2 m are

Optics EXPRESS

presented in Fig. 4(b), in which the maximal value at the vicinity of the near-zero dispersion frequencies (128 GHz and 140 GHz) are capped with BR_{ZD}. It can be seen that the maximum error-free transmission bit rate of ~17 Gbps can be supported by the X-polarized mode at 128 GHz, meanwhile, the Y-polarized mode can also support a bit rate of ~19 Gbps at 128 GHz. More interestingly, for the Y-polarized mode, the maximum error-free transmission bit rate of ~26 Gbps can be obtained in the vicinity of the corresponding near-zero dispersion frequency (140 GHz). The excellent performance of the Y-polarized mode in terms of the achievable maximum bit rate is due to its smaller dispersion slope (compared to the X-polarization) as seen from the dispersion curve in Fig. 4(a). In general, for the transmission fiber, the dispersion should be designed to be small and its dispersion slope should be constant (the curvature of the dispersion curve is close to zero), while the dispersion-compensating fiber should have a high dispersion value and a dispersion slope matching that of the transmission fiber in order to broaden the channel bandwidth [120].

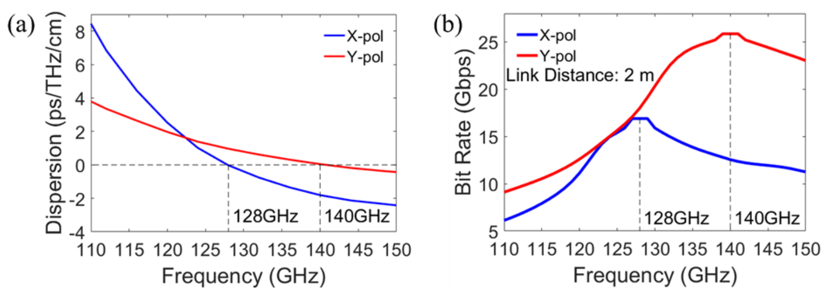

Fig. 4. (a) Second-order dispersion of the X-polarized and Y-polarized modes as a function of frequency. (b) Maximum bit rate supported by the X-polarized and Y-polarized modes for the link length of 2 m.

4. Experimental characterization of the PMF communication link

The experimental characterization of the two orthogonally polarized fundamental modes for the PMF was carried out using the photonics-based THz communication system detailed in our previous work [50]. For the transmission loss and the crosstalk measurements, and the near-field imaging, the system was used in the continuous wave (CW) THz spectroscopy mode (see Supplement 1 Sec. S4) by disabling the communication unit. The bit error rate (BER) measurements for the two modes were carried out with the system in the THz communication mode (see Supplement 1 Sec. S5) by activating the communication unit.

4.1. Transmission loss and crosstalk measurements

The transmission losses of the two orthogonally polarized fundamental modes for the PMF were measured using a cut-back method with the CW THz spectroscopy system. The PMF input facet was fixed during the measurements, while the orientation and position of the transmitter were first optimized to excite either X-polarized or Y-polarized mode and kept unchanged during the following measurements. After each fiber cut, the position and orientation of the receiver were optimized to detect maximal power (see Supplement 1 Sec. S4). As a result, a total of 7 transmission spectra in the range of 110-150 GHz were obtained for each polarization and the PMF lengths of 1.6-3 m [see Figs. 5(a) and 5(b)]. The frequency (ν) dependent fiber losses $\alpha_{Ti}^{Ri}(\nu)$, $(i = \text{"}x\text{" } or \text{ "}y\text{"})$ for the two modes are estimated by minimizing the least-squares deviation of the experimentally measured transmission spectra P_{Ti}^{Ri} from their theoretical fit in the

Optics EXPRESS

following form:

$$P^{Ri}_{Ti} = P_0 \cdot exp(-\alpha^{Ri}_{Ti}(\nu)L)$$
$$\alpha^{Ri}_{Ti}(\nu) = a_2\nu^2 + a_1\nu + a_0, \quad i = \text{"}x\text{" } or \text{ "}y\text{"} \tag{5}$$

The experimental transmission losses and their theoretical fits for the X-polarized and Y-polarized modes are shown as the blue and red solid curves in Figs. 5(c) and 5(d). Additionally, in red dashed curves we show theoretically computed modal losses found using COMSOL mode solver while choosing the effective fiber material losses as ~5.11·α_{PP} for the X-polarized mode, and ~5.76·α_{PP} for the Y-polarized mode in order to best match the experimental losses. A good agreement between the experimental and theoretical transmission losses is found for both polarizations. In the 110-150 GHz spectral range, the experimental losses of the PMF are found to vary between ~7.7-15.5 dB/m and ~9.4-17.9 dB/m for the X-polarized and Y-polarized modes respectively. At the optimal operating frequency of our THz communication system of 128 GHz, the corresponding losses are ~10.9 dB/m and ~12.9 dB/m.

Next, we study crosstalk in our polarization-maintaining fiber. The crosstalk figure of merit can be used to judge the efficacy of a PMF to maintain a given linear polarization state. It was measured for fibers of lengths between 1.6-2 m that were later used in the data transmission measurements. The crosstalk is measured by comparing the received power in the mode of undesired polarization (P^{Rj}_{Ti}) to the power in the mode of the principal polarization (P^{Ri}_{Ti}) [Figs. 5(a) and 5(b)]:

$$Crosstalk^{j}_{i} = 10{*}log_{10}(P^{Rj}_{Ti}/P^{Ri}_{Ti})$$
$$i,j = \text{x } or \text{ y}$$
$$i \neq j \tag{6}$$

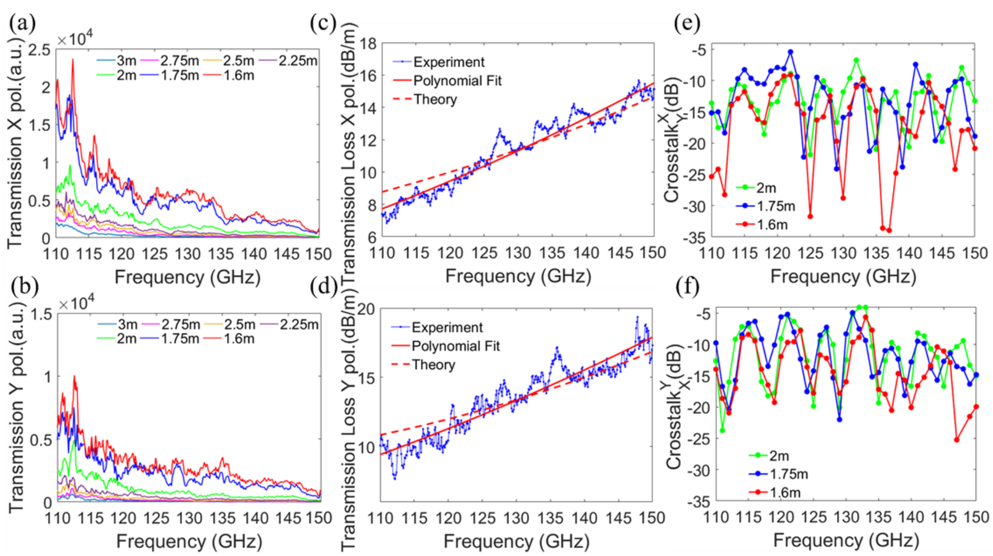

Fig. 5. (a) Transmission spectra (P^{Rx}_{Tx}) of the X-polarized mode under optimal excitation conditions using a WR-6 waveguide. (b) Transmission spectra (P^{Ry}_{Ty}) of the Y-polarized mode under optimal excitation conditions using a WR-6 waveguide. Experimental transmission losses (by power) of the (c) X-polarized and (d) Y-polarized mode. Experimental crosstalk when transmitting (e) X-polarized and (f) Y-polarized modes in the PMFs of different lengths.

Optics EXPRESS

The measured crosstalk is presented in Figs. 5(e) and 5(f). From the figures, we observe that the crosstalk value when operating in the X-polarized mode of a several-meter-long fiber is ~14.5±5.2 dB, which is somewhat higher than ~12.7±4.5 dB when operating in the Y-polarized mode. The polarization crosstalk in our fibers is mainly caused by the imperfections and shape variations of the internal structures (core and bridges) along the fiber length (see Supplement 1 Sec. S3). The crosstalk is somewhat higher for the Y-polarized mode as the mode has a significant presence in thin bridges for which the effect of imperfections is more pronounced than for the case of a relatively large core where most of the X-polarized mode is concentrated. Nevertheless, the relatively low average crosstalk values of ~14.5 dB and ~12.7 dB for X and Y polarizations, respectively, demonstrate that our PMF can successfully maintain the polarization state over practically useful fiber lengths of ~2 m.

4.2. Improvement of the fiber transmission loss by annealing

Next, we studied the effects of annealing on the fiber's optical properties. Particularly, three 25 cm-long fiber sections obtained during the cut-back measurement were annealed in a vacuum furnace at a temperature close to the melting point (~ 150 °C) of the fiber material (PP), thus allowing the fiber to soften enough to achieve surface relaxation and defect closure driven by the polymer surface tension while avoiding structural deformation (see Supplement 1 Sec. S3). The fiber transmission losses of the X- and Y-polarized modes of the three fiber sections (Fibers I-III) before and after annealing (1-5 days) are presented in Fig. 6. They were measured by comparing the reference signal at the fiber input end with the signal at the fiber output end as in a standard cut-back measurement. Namely, to eliminate the effect of coupling losses, the 25 cm-long fiber sections were mechanically spliced with a 10 cm-long reference fiber section (not annealed) using a hexagonal connector/holder, while the out-coupling conditions were optimized by rotating the detector and scanning the fiber with the WR6 waveguide at the fiber output facet (see Supplement 1 Sec. S4 for details).

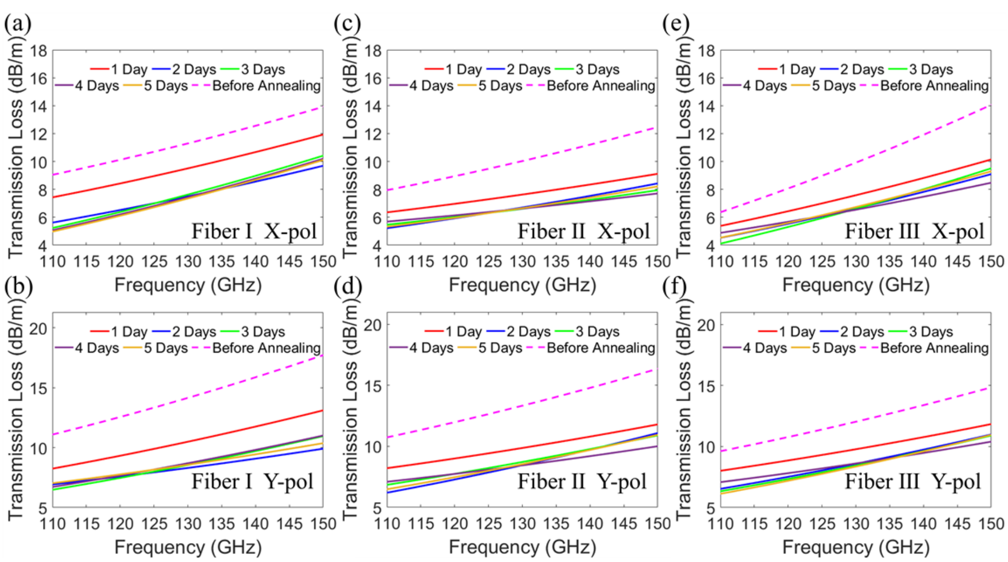

Fig. 6. Experimental transmission losses of the 0.25 m-long fiber sections for the X and Y polarizations. Data for the fiber section (a)(b) I, (c)(d) II, and (e)(f) III after 1-5 days of annealing.

Optics EXPRESS

The reference signals (for the X and Y polarizations) were recorded at the output end of a 10 cm-long reference section which was fixed throughout the experiment, while the position and inclination of the emitter were maintained at the optimal excitation conditions for each polarization.

The differences in transmission losses of the three fiber sections as seen in Fig. 6 are mainly due to somewhat different excitation conditions at the fiber input facets (see Supplement 1 Sec. S3) during measurements. In Fig. 6, we can see that the transmission losses of the X-polarized and Y-polarized modes are reduced by ~2.7-4.4 dB/m and ~3.8-5.6 dB/m in the 110-150 GHz range for all three fiber sections after ~2 days of annealing, while longer annealing times do not contribute significantly to the further loss reduction.

While the further investigation of the effect of annealing on the 3D-printed fiber performance is in order, from these preliminary results we conclude that annealing is indeed a potent technique that could significantly reduce the printed waveguide transmission losses. In the case of the infinity 3D printers, further work is still required to combine printing and annealing into a single continuous process.

4.3. Communication demonstration using PMF before and after annealing

Next, the communication performance of the 1.6 m-long PMF before and after annealing was evaluated using a photonics-based THz communication system (see Supplement 1 Sec. S5) by measuring the BER for various data rates at the carrier frequency of 128 GHz. The maximal fiber length for communication experiments was limited by the relatively low emitter output power (~218 μW), as well as relatively high fiber transmission losses. The fiber length of 1.6 m was chosen so that the signal strength in the X polarization of a non-annealed fiber is high enough to result in the BER at the level of a forward error correction (FEC) limit of ~10^{-3}. Then, after annealing, it was found that the signal strengths in both the X and Y polarizations were improved greatly, and BER measurements were repeated. The measured BERs of the X-polarized and Y-polarized modes for both annealed and non-annealed fibers are presented in Fig. 7(a). From the figure, we observe that before annealing the BER of the Y-polarized mode cannot be measured due to the weak strength of the received signal [see the corresponding eye pattern in Fig. 7(b)]. Meanwhile, the BER when

using the X-polarized mode of the non-annealed fiber is measurable and it is in the ~10^{-5}-10^{-2} range with the received power ~10 times higher than the noise floor. Next, the BER measurements were repeated after annealing the fiber at ~140°C using an ~80 cm-long tubular furnace (Model: PS205-208-(3)25-P-K from Mellen Inc.) with fiberglass insulation placed at both ends. The annealing process was conducted on the continuous 1.6 m-long fiber in 4 steps by threading

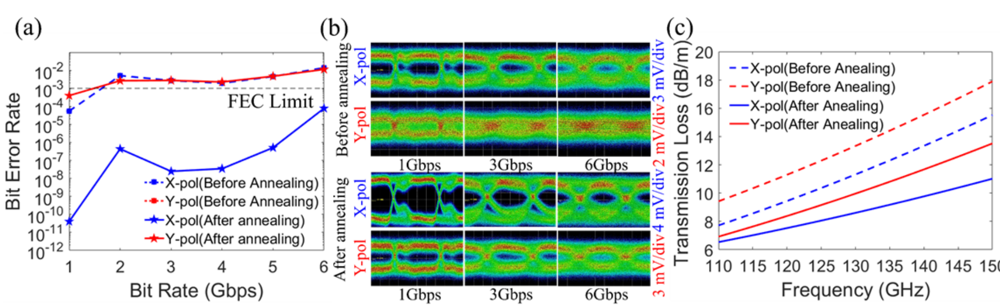

Fig. 7. (a) Measured Bit Error Rate versus Bit Rate and (b) Recorded Eye Pattern versus Bit Rates for the X-polarized and Y-polarized modes of the 1.6 m-long PMF before and after annealing at the carrier frequency of 128 GHz. (c) Experimental transmission losses of the PMF before and after annealing were measured using the cut-back method.

Optics EXPRESS

the fiber through the furnace in 0.4 m intervals and individually annealing each section. As a result, the communication performance of the fiber was greatly improved due to significantly reduced transmission losses for both polarizations [see the eye patterns and transmission losses of the PMF after annealing in Figs. 7(b) and 7(c)]. Thus, the BER of the Y-polarized mode became measurable and reached ~10^{-4}-10^{-2}, while the BER of the X-polarized mode was greatly improved to ~10^{-11}-10^{-5} for the data rates of 1-6 Gbps.

4.4. Mode field imaging of the two orthogonally polarized modes of the PMF

Finally, the near-field modal imaging has been carried out at the PMF output end using the CW THz spectroscopy system (see Supplement 1 Sections S4 and S6) to visualize field amplitude distributions of the two orthogonally polarized modes of the fabricated PMF (see Fig. 8). The PMF was fixed throughout the measurements, while the polarization directions of the transmitter and receiver were rotated horizontally or vertically to visualize the X- or Y-polarized modes. The theoretical modal field distributions were computed by importing the microscopy photo of a real waveguide cross-section into COMSOL Multiphysics and then computing the modes of a corresponding waveguide. The red arrows in the theoretical modal field distributions indicate the electric field directions of the fundamental modes, while the red arrows in the experimental images are the electric field directions of the fundamental modes in the WR-6 waveguide. Overall, we observe a reasonable correspondence between the theoretical and experimental modal images, especially for the X-polarized mode, while the difference between theory and experiment is more significant for the Y-polarized mode. Remarkably, experimental images do not show a significant presence of the modal fields in the four thin bridges that support the core, while theoretical images do. This difference can be justified by noting that numerical images are obtained assuming that the waveguide cross-section is constant along the fiber length, while in practice it is not the case due to the nature of the layer-by-layer printing process. We, therefore, believe that the modal fields in the thin bridges are strongly irradiated by the periodic imperfections (along the fiber length) imposed by the printing process, while their effect on the modal field in a much larger core is significantly less pronounced.

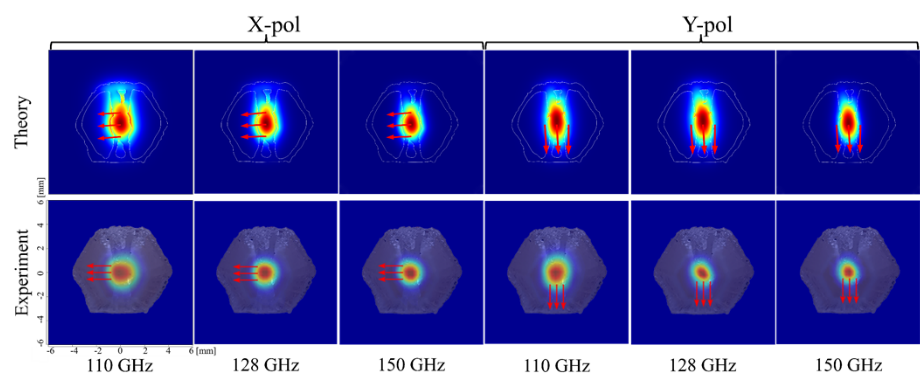

Fig. 8. Comparison of the numerically computed and experimentally measured electric field distributions of the X-polarized and Y-polarized modes at the end of the 1.6 m-long PMF. Red arrows represent the electric field directions. In experimental measurements, the electric field direction is defined by the orientation of the WR-6 waveguide flange.

5. Conclusion

In this work, we studied numerically and experimentally polarization maintaining THz fibers designed to have low group velocity dispersion and high inter-modal birefringence. By utilizing

Optics EXPRESS

the novel infinity 3D printing technique, the 5 m-long fiber was fabricated in a continuous printing process with losses of ~7.7-15.5 dB/m for X polarization and ~9.4-17.9 dB/m for Y polarization in the 110-150 GHz spectral range.

Moreover, a significant reduction of the fiber transmission losses was demonstrated after annealing the printed fiber at a temperature close to the fiber material melting point, resulting in improved transmission losses of ~6.5-11 dB/m for the X polarization and ~6.9-13.5 dB/m for the Y polarization in the 110-150 GHz range. Significant improvement in the fiber quality after annealing was also verified by characterizing BER in the real-time data transmission links using a 1.6 m-long PMF. For X polarization, in particular, the measurements show improved BERs of ~10^{-11}-10^{-5} after annealing compared to ~10^{-4}-10^{-2} before annealing for the 1-6 Gbps data rates at 128 GHz carrier frequency.

Furthermore, the ability of the PMF to maintain a linear polarization state during transmission was evaluated by experimentally measuring the inter-polarization crosstalk. The measured average crosstalk was ~14.5 dB for X polarization and ~12.7 dB for Y polarization, which demonstrates good polarization-maintaining properties of the infinity 3D printed PMF even in the presence of manufacturing imperfections.

The results of this work show that infinity 3D printing supplemented with post-fabrication annealing is a powerful technique for the continuous fabrication of the THz fibers of complex transverse geometries and advanced optical properties.

Funding. Canada Research Chairs Tier I in Ubiquitous THz Photonics of Prof. M. Skorobogatiy.

Acknowledgments. We thank our technicians Mr. Jean-Paul Lévesque and Mr. Yves Leblanc for their assistance.

Disclosures. The authors declare that there are no conflicts of interest related to this article.

Data availability. Data underlying the results presented in this paper are not publicly available at this time but may be obtained from the authors upon reasonable request.

Supplemental document. See Supplement 1 for supporting content.

References

1. K. Fukunaga, N. Sekine, I. Hosako, N. Oda, H. Yoneyama, and T. Sudoh, "Real-time terahertz imaging for art conservation science," J. Eur. Opt. Soc.: Rapid Publications **3**, 08027 (2008).
2. H. Guerboukha, K. Nallappan, and M. Skorobogatiy, "Toward real-time terahertz imaging," Adv. Opt. Photonics **10**(4), 843–938 (2018).
3. R. Henri, K. Nallappan, D. S. Ponomarev, H. Guerboukha, D. V. Lavrukhin, A. E. Yachmenev, R. A. Khabibullin, and M. Skorobogatiy, "Fabrication and Characterization of an 8× 8 Terahertz Photoconductive Antenna Array for Spatially Resolved Time Domain Spectroscopy and Imaging Applications," IEEE Access **9**, 117691–117702 (2021).
4. E. Castro-Camus, M. Koch, and D. M. Mittleman, "Recent advances in terahertz imaging: 1999 to 2021," Appl. Phys. B **128**(1), 12 (2022).
5. Y. Cao, K. Nallappan, H. Guerboukha, T. Gervais, and M. Skorobogatiy, "Additive manufacturing of resonant fluidic sensors based on photonic bandgap waveguides for terahertz applications," Opt. Express **27**(20), 27663–27681 (2019).
6. M. Poulin, S. Giannacopoulos, and M. Skorobogatiy, "Surface Wave Enhanced Sensing in the Terahertz Spectral Range: Modalities, Materials, and Perspectives," Sensors **19**(24), 5505 (2019).
7. G. M. Katyba, K. I. Zaytsev, N. V. Chernomyrdin, I. A. Shikunova, G. A. Komandin, V. B. Anzin, S. P. Lebedev, I. E. Spektor, V. E. Karasik, and S. O. Yurchenko, "Sapphire photonic crystal waveguides for terahertz sensing in aggressive environments," Adv. Opt. Mater. **6**(22), 1800573 (2018).
8. J. Ornik, D. Knoth, C. M. Keck, and M. Koch, "Potential of THz-TDS for Crystallinity State Inspection of Active Pharmaceutical Ingredients in SmartFilms®," in *2020 45th International Conference on Infrared, Millimeter, and Terahertz Waves (IRMMW-THz)* (IEEE, 2020), 1–2.
9. J. F. Federici, B. Schulkin, F. Huang, D. Gary, R. Barat, F. Oliveira, and D. Zimdars, "THz imaging and sensing for security applications—explosives, weapons and drugs," Semicond. Sci. Technol. **20**(7), S266–S280 (2005).
10. Y. C. Shen, T. Lo, P. F. Taday, B. E. Cole, W. R. Tribe, and M. C. Kemp, "Detection and identification of explosives using terahertz pulsed spectroscopic imaging," Appl. Phys. Lett. **86**(24), 24116 (2005).
11. N. Laman, S. S. Harsha, D. Grischkowsky, and J. S. Melinger, "7 GHz resolution waveguide THz spectroscopy of explosives related solids showing new features," Opt. Express **16**(6), 4094–4105 (2008).
12. K. Nallappan, H. Guerboukha, C. Nerguizian, and M. Skorobogatiy, "Live Streaming of Uncompressed HD and 4 K Videos Using Terahertz Wireless Links," IEEE Access **6**, 58030–58042 (2018).
13. M. A. Akkaş, "Terahertz wireless data communication," Wireless Netw. **25**(1), 145–155 (2019).

14. K. Nallappan, H. Guerboukha, Y. Cao, G. Xu, C. Nerguizian, M. Daniel M, and M. Skorobogatiy, "Terahertz Waveguides for Next Generation Communication Network: Needs, Challenges and Perspectives," in *Next Generation Wireless Terahertz Communication Networks*, S. Ghafoor, M. H. Rehmani, and A. Davy, eds. (CRC Press, 2021).
15. M. Nagel, P. Haring Bolivar, M. Brucherseifer, H. Kurz, A. Bosserhoff, and R. Büttner, "Integrated THz technology for label-free genetic diagnostics," Appl. Phys. Lett. **80**(1), 154–156 (2002).
16. J. B. Jensen, P. E. Hoiby, G. Emiliyanov, O. Bang, L. H. Pedersen, and A. Bjarklev, "Selective detection of antibodies in microstructured polymer optical fibers," Opt. Express **13**(15), 5883–5889 (2005).
17. R. Woodward, V. Wallace, D. Arnone, E. Linfield, and M. Pepper, "Terahertz pulsed imaging of skin cancer in the time and frequency domain," J. Biological Phys. **29**(2/3), 257–259 (2003).
18. R. M. Woodward, B. E. Cole, V. P. Wallace, R. J. Pye, D. D. Arnone, E. H. Linfield, and M. Pepper, "Terahertz pulse imaging in reflection geometry of human skin cancer and skin tissue," Phys. Med. Biol. **47**(21), 3853–3863 (2002).
19. O. P. Cherkasova, D. S. Serdyukov, E. F. Nemova, A. S. Ratushnyak, A. S. Kucheryavenko, I. N. Dolganova, G. Xu, M. Skorobogatiy, I. V. Reshetov, and P. S. Timashev, "Cellular effects of terahertz waves," J. Biomed. Opt. **26**(9), 090902 (2021).
20. J. B. Carruthers, "Wireless infrared communications," Proc. IEEE **85**(2), 265–298 (1997).
21. K. Chang, *RF and Microwave Wireless Systems* (John Wiley & Sons, 2004).
22. D. C. O'Brien, G. E. Faulkner, K. Jim, E. B. Zyambo, D. J. Edwards, M. Whitehead, P. Stavrinou, G. Parry, J. Bellon, and M. J. Sibley, "High-speed integrated transceivers for optical wireless," IEEE Commun. Mag. **41**(3), 58–62 (2003).
23. T. S. Rappaport, Y. Xing, O. Kanhere, S. Ju, A. Madanayake, S. Mandal, A. Alkhateeb, and G. C. Trichopoulos, "Wireless communications and applications above 100 GHz: Opportunities and challenges for 6 G and beyond," IEEE Access **7**, 78729–78757 (2019).
24. J. Ma, R. Shrestha, L. Moeller, and D. M. Mittleman, "Invited article: Channel performance for indoor and outdoor terahertz wireless links," APL Photonics **3**(5), 051601 (2018).
25. T. S. Rappaport, S. Sun, R. Mayzus, H. Zhao, Y. Azar, K. Wang, G. N. Wong, J. K. Schulz, M. Samimi, and F. Gutierrez, "Millimeter wave mobile communications for 5 G cellular: It will work!" IEEE Access **1**, 335–349 (2013).
26. J. A. Shaw, "Radiometry and the Friis transmission equation," Am. J. Phys. **81**(1), 33–37 (2013).
27. R. Piesiewicz, M. Jacob, M. Koch, J. Schoebel, and T. Kurner, "Performance Analysis of Future Multigigabit Wireless Communication Systems at THz Frequencies With Highly Directive Antennas in Realistic Indoor Environments," IEEE J. Sel. Top. Quantum Electron. **14**(2), 421–430 (2008).
28. H. Elayan, O. Amin, B. Shihada, R. M. Shubair, and M.-S. Alouini, "Terahertz Band: The Last Piece of RF Spectrum Puzzle for Communication Systems," IEEE Open J. Commun. Soc. **1**, 1–32 (2020).
29. T. Kleine-Ostmann and T. Nagatsuma, "A Review on Terahertz Communications Research," J. Infrared, Millimeter, and Terahertz Waves **32**(2), 143–171 (2011).
30. Y. Mei, Y. Ma, J. Ma, L. Moeller, and J. F. Federici, "Eavesdropping risk evaluation on terahertz wireless channels in atmospheric turbulence," IEEE Access **9**, 101916–101923 (2021).
31. R. Wang, Y. Mei, X. Meng, and J. Ma, "Secrecy performance of terahertz wireless links in rain and snow," Nano Commun. Netw. **28**, 100350 (2021).
32. J. Ma, R. Shrestha, J. Adelberg, C.-Y. Yeh, Z. Hossain, E. Knightly, J. M. Jornet, and D. M. Mittleman, "Security and eavesdropping in terahertz wireless links," Nature **563**(7729), 89–93 (2018).
33. K. Tsuruda, T. Ishigaki, A. Suminokura, R. Kakimi, M. Fujita, and T. Nagatsuma, "Ultralow-loss photonic-crystal waveguides for gigabit terahertz-wave communications," in *2013 IEEE International Topical Meeting on Microwave Photonics (MWP)* (IEEE, 2013), 9–12.
34. K. Tsuruda, M. Fujita, and T. Nagatsuma, "Extremely low-loss terahertz waveguide based on silicon photonic-crystal slab," Opt. Express **23**(25), 31977–31990 (2015).
35. X. Yu, M. Sugeta, Y. Yamagami, M. Fujita, and T. Nagatsuma, "Simultaneous low-loss and low-dispersion in a photonic-crystal waveguide for terahertz communications," Appl. Phys. Express **12**(1), 012005 (2019).
36. Y. Yang, Y. Yamagami, X. Yu, P. Pitchappa, J. Webber, B. Zhang, M. Fujita, T. Nagatsuma, and R. Singh, "Terahertz topological photonics for on-chip communication," Nat. Photonics **14**(7), 446–451 (2020).
37. W. Gao, X. Yu, M. Fujita, T. Nagatsuma, C. Fumeaux, and W. Withayachumnankul, "Effective-medium-cladded dielectric waveguides for terahertz waves," Opt. Express **27**(26), 38721–38734 (2019).
38. B. Yu, Y. Ye, X. Ding, C. Neher, X. Liu, Z. Xu, and Q. J. Gu, "Sub-THz interconnect for planar chip-to-chip communications," in *2018 IEEE 18th Topical Meeting on Silicon Monolithic Integrated Circuits in RF Systems (SiRF)* (IEEE, 2018), 54–56.
39. B. Yu, Y. Ye, X. Ding, Y. Liu, Z. Xu, X. Liu, and Q. J. Gu, "Ortho-Mode Sub-THz Interconnect Channel for Planar Chip-to-Chip Communications," IEEE Trans. Microwave Theory Techn. **66**(4), 1864–1873 (2018).
40. M. Sawaby, N. Dolatsha, B. Grave, C. Chen, and A. Arbabian, "A Fully Packaged 130-GHz QPSK Transmitter With an Integrated PRBS Generator," IEEE Solid-State Circuits Lett. **1**(7), 166–169 (2018).
41. M. De Wit, Y. Zhang, and P. Reynaert, "Analysis and Design of a Foam-Cladded PMF Link With Phase Tuning in 28-nm CMOS," IEEE J. Solid-State Circuits **54**(7), 1960–1969 (2019).

42. J. W. Holloway, G. C. Dogiamis, and R. Han, "A 105Gb/s Dielectric-Waveguide Link in 130 nm BiCMOS Using Channelized 220-to-335 GHz Signal and Integrated Waveguide Coupler," in *2021 IEEE International Solid- State Circuits Conference (ISSCC)* (2021), pp. 196–198.
43. M. Tytgat and P. Reynaert, "A plastic waveguide receiver in 40 nm CMOS with on-chip bondwire antenna," in *2013 Proceedings of the ESSCIRC (ESSCIRC)* (IEEE, 2013), 335–338.
44. M. Tytgat, N. Van Thienen, and P. Reynaert, "A 90-GHz receiver in 40-nm CMOS for plastic waveguide links," Analog Integrated Circuits and Signal Process. **83**(1), 55–64 (2015).
45. B. Yu, Y. Ye, X. L. Liu, and Q. J. Gu, "Microstrip line based sub-THz interconnect for high energy-efficiency chip-to-chip communications," in *2016 IEEE International Symposium on Radio-Frequency Integration Technology (RFIT)* (IEEE, 2016), 1–3.
46. X. Yu, T. Miyamoto, K. Obata, Y. Hosoda, J.-Y. Kim, M. Fujita, and T. Nagatsuma, "Direct terahertz communications with wireless and fiber links," in *2019 44th International Conference on Infrared, Millimeter, and Terahertz Waves (IRMMW-THz)* (IEEE, 2019), 1–2.
47. J. Yu, X. Li, X. Tang, H. Zhang, N. Chi, and Y. Shi, "High-Speed Signal Transmission at W-Band Over Dielectric-Coated Metallic Hollow Fiber," IEEE Trans. Microwave Theory and Techn. **63**(6), 1836–1842 (2015).
48. W. Volkaerts, N. Van Thienen, and P. Reynaert, "An FSK plastic waveguide communication link in 40 nm CMOS," in *2015 IEEE International Solid-State Circuits Conference-(ISSCC) Digest of Technical Papers* (IEEE, 2015), 1–3.
49. N. Van Thienen, W. Volkaerts, and P. Reynaert, "A Multi-Gigabit CPFSK Polymer Microwave Fiber Communication Link in 40 nm CMOS," IEEE J. Solid-State Circuits **51**(8), 1952–1958 (2016).
50. K. Nallappan, Y. Cao, G. Xu, H. Guerboukha, C. Nerguizian, and M. Skorobogatiy, "Dispersion Limited versus Power Limited Terahertz Transmission Links Using Solid Core Subwavelength Dielectric Fibers," Photonics Res. **8**(11), 1757–1775 (2020).
51. K. Nallappan, Y. Cao, G. Xu, H. Guerboukha, C. Nerguizian, and M. Skorobogatiy, "Increasing Reliability of Terahertz Communication Links Using Onboard Fiber Connectivity," in *2020 10th Annual Computing and Communication Workshop and Conference (CCWC)* (IEEE, 2020), 1065–1070.
52. K. Nallappan and M. Skorobogatiy, "Wired Channel Modeling for Frequency Hopping System in Secure Terahertz Communications," in *2021 IEEE Research and Applications of Photonics in Defense Conference (RAPID)* (2021), pp. 1–2.
53. K. Nallappan and M. Skorobogatiy, "Comparison of Wired and Wireless Channel for Short Range Frequency Hopping Terahertz System," in *2021 IEEE Photonics Society Summer Topicals Meeting Series (SUM)* (2021), pp. 1–2.
54. G. Xu, K. Nallappan, Y. Cao, and M. Skorobogatiy, "Infinity additive manufacturing of continuous microstructured fiber links for THz communications," Sci. Rep. **12**(1), 4551 (2022).
55. K. Dens, J. Vaes, S. Ooms, M. Wagner, and P. Reynaert, "A PAM4 Dielectric Waveguide Link in 28 nm CMOS," in *ESSCIRC 2021-IEEE 47th European Solid State Circuits Conference (ESSCIRC)* (IEEE, 2021), 479–482.
56. K. Nallappan, H. Guerboukha, Y. Cao, C. Nerguizian, and M. Skorobogatiy, "Experimental demonstration of 5 Gbps data transmission using long subwavelength fiber at 140 GHz," in *2019 IEEE Radio and Wireless Symposium (RWS)* (IEEE, 2019), 1–4.
57. J. Ma, M. Weidenbach, R. Guo, M. Koch, and D. M. Mittleman, "Communications with THz Waves: Switching Data Between Two Waveguides," J. Infrared Milli. Terahz Waves **38**(11), 1316–1320 (2017).
58. M. Yata, M. Fujita, and T. Nagatsuma, "Photonic-crystal diplexers for terahertz-wave applications," Opt. Express **24**(7), 7835–7849 (2016).
59. D. Headland, W. Withayachumnankul, X. Yu, M. Fujita, and T. Nagatsuma, "Unclad Microphotonics for Terahertz Waveguides and Systems," J. Lightwave Technol. **38**(24), 1 (2020).
60. D. Headland, W. Withayachumnankul, M. Fujita, and T. Nagatsuma, "Gratingless integrated tunneling multiplexer for terahertz waves," Optica **8**(5), 621–629 (2021).
61. Y. Cao, K. Nallappan, H. Guerboukha, G. Xu, and M. Skorobogatiy, "Additive manufacturing of highly reconfigurable plasmonic circuits for terahertz communications," Optica **7**(9), 1112–1125 (2020).
62. J. Dong, A. Tomasino, G. Balistreri, P. You, A. Vorobiov, E. Charette, B. Le Drogoff, M. Chaker, A. Yurtsever, S. Stivala, M. A. Vincenti, C. De Angelis, D. Kip, J. Azana, and R. Morandotti, "Versatile metal-wire waveguides for broadband terahertz signal processing and multiplexing," Nat. Commun. **13**(1), 741 (2022).
63. Y. Cao, K. Nallappan, G. Xu, and M. Skorobogatiy, "Add drop multiplexers for terahertz communications using two-wire waveguide based plasmonic circuits," arXiv, arXiv:2107.14090 (2021).
64. T. Ma, K. Nallapan, H. Guerboukha, and M. Skorobogatiy, "Analog signal processing in the terahertz communication links using waveguide Bragg gratings: example of dispersion compensation," Opt. Express **25**(10), 11009–11026 (2017).
65. G. Xu and M. Skorobogatiy, "Wired THz Communications," J. Infrared Milli. Terahz Waves **43**(9-10), 728–778 (2022).
66. T. Ma, A. Markov, L. Wang, and M. Skorobogatiy, "Graded index porous optical fibers - dispersion management in terahertz range," Opt. Express **23**(6), 7856–7869 (2015).
67. A. Dupuis, A. Mazhorova, F. Desevedavy, M. Roze, and M. Skorobogatiy, "Spectral characterization of porous dielectric subwavelength THz fibers fabricated using a microstructured molding technique," Opt. Express **18**(13), 13813–13828 (2010).

68. J. Noda, K. Okamoto, and Y. Sasaki, “Polarization-maintaining fibers and their applications,” J. Lightwave Technol. **4**(8), 1071–1089 (1986).
69. Z. Yu, C. Hou, Y. Yuan, P. Xu, X. Dong, J. Yang, L. Yuan, Y. Wang, and Y. Qin, “High Accuracy Distributed Polarization Extinction Ratio Measurement For a Polarization-Maintaining Device With Strong Polarization Crosstalk,” J. Lightwave Technol. **39**(7), 2177–2186 (2021).
70. E. Reyes-Vera, J. Usuga-Restrepo, C. Jimenez-Durango, J. Montoya-Cardona, and N. Gomez-Cardona, “Design of Low-loss and Highly Birefringent Porous-Core Photonic Crystal Fiber and Its Application to Terahertz Polarization Beam Splitter,” IEEE Photonics J. **10**(4), 1–13 (2018).
71. M. R. Islam, M. F. Kabir, K. M. A. Talha, and M. S. Arefin, “Highly birefringent honeycomb cladding terahertz fiber for polarization-maintaining applications,” Opt. Eng. **59**(1), 016113 (2020).
72. R. Islam, M. S. Habib, G. Hasanuzzaman, S. Rana, and M. A. Sadath, “Novel porous fiber based on dual-asymmetry for low-loss polarization maintaining THz wave guidance,” Opt. Lett. **41**(3), 440–443 (2016).
73. J. Luo, F. Tian, H. Qu, L. Li, J. Zhang, X. Yang, and L. Yuan, “Design and numerical analysis of a THz square porous-core photonic crystal fiber for low flattened dispersion, ultrahigh birefringence,” Appl. Opt. **56**(24), 6993–7001 (2017).
74. R. Islam, M. S. Habib, G. K. M. Hasanuzzaman, S. Rana, M. A. Sadath, and C. Markos, “A Novel Low-Loss Diamond-Core Porous Fiber for Polarization Maintaining Terahertz Transmission,” IEEE Photonics Technol. Lett. **28**(14), 1537–1540 (2016).
75. Y. Zhang, L. Xue, D. Qiao, and Z. Guang, “Porous photonic-crystal fiber with near-zero ultra-flattened dispersion and high birefringence for polarization-maintaining terahertz transmission,” Optik **207**, 163817 (2020).
76. Y. Zhang, X. Jing, D. Qiao, and L. Xue, “Rectangular Porous-Core Photonic-Crystal Fiber With Ultra-Low Flattened Dispersion and High Birefringence for Terahertz Transmission,” Front. Phys. **8**, 370 (2020).
77. M. R. Hasan, M. S. Anower, M. I. Hasan, and S. M. A. Razzak, “Polarization Maintaining Low-Loss Slotted Core Kagome Lattice THz Fiber,” IEEE Photonics Technol. Lett. **28**(16), 1751–1754 (2016).
78. D.-D. Wang, C.-L. Mu, D.-P. Kong, and C.-Y. Guo, “High birefringence, low loss, and flattened dispersion photonic crystal fiber for terahertz application,” Chin. Phys. B **28**(11), 118701 (2019).
79. S. Rana, N. Kandadai, and H. Subbaraman, “A Highly Sensitive, Polarization Maintaining Photonic Crystal Fiber Sensor Operating in the THz Regime,” Photonics **5**(4), 40 (2018).
80. R. Islam, M. S. Habib, G. K. M. Hasanuzzaman, R. Ahmad, S. Rana, and S. F. Kaijage, “Extremely High-Birefringent Asymmetric Slotted-Core Photonic Crystal Fiber in THz Regime,” IEEE Photonics Technol. Lett. **27**(21), 2222–2225 (2015).
81. M. Rabiul Hasan, M. Shamim Anower, M. Ariful Islam, and S. M. Razzak, “Polarization-maintaining low-loss porous-core spiral photonic crystal fiber for terahertz wave guidance,” Appl. Opt. **55**(15), 4145–4152 (2016).
82. F. A. Mou, M. M. Rahman, M. A. Al Mahmud, M. R. Islam, and M. I. H. Bhuiyan, “Design and characterization of a low loss polarization maintaining photonic crystal fiber for THz regime,” in *2019 IEEE International Conference on Telecommunications and Photonics (ICTP)* (IEEE, 2019), 1–4.
83. H. Kaveh, F. Jahangiri, and T. Amini, “Silicon nitride based photonic crystal fiber with highly improved birefringence for low loss terahertz propagation,” Opt. Continuum **1**(2), 388–398 (2022).
84. G. K. M. Hasanuzzaman, S. Rana, and M. S. Habib, “A Novel Low Loss, Highly Birefringent Photonic Crystal Fiber in THz Regime,” IEEE Photonics Technol. Lett. **28**(8), 899–902 (2016).
85. K. Ahmed, S. Chowdhury, B. K. Paul, M. Shadidul Islam, S. Sen, M. Ibadul Islam, and S. Asaduzzaman, “Ultrahigh birefringence, ultralow material loss porous core single-mode fiber for terahertz wave guidance,” Appl. Opt. **56**(12), 3477–3483 (2017).
86. G. Ren, Y. Gong, P. Shum, X. Yu, J. Hu, G. Wang, M. O. L. Chuen, and V. Paulose, “Low-loss air-core polarization maintaining terahertz fiber,” Opt. Express **16**(18), 13593–13598 (2008).
87. S. Li, H. Liu, N. Huang, and Q. Sun, “Broadband high birefringence and low dispersion terahertz photonic crystal fiber,” J. Opt. **16**(10), 105102 (2014).
88. G. Ren, Y. Gong, P. Shum, X. Yu, and J. Hu, “Polarization Maintaining Air-Core Bandgap Fibers for Terahertz Wave Guiding,” IEEE J. Quantum Electron. **45**(5), 506–513 (2009).
89. M. Sharma, N. Borogohain, and S. Konar, “Index Guiding Photonic Crystal Fibers With Large Birefringence and Walk-Off,” J. Lightwave Technol. **31**(21), 3339–3344 (2013).
90. Z. Wu, Z. Shi, H. Xia, X. Zhou, Q. Deng, J. Huang, X. Jiang, and W. Wu, “Design of Highly Birefringent and Low-Loss Oligoporous-Core THz Photonic Crystal Fiber With Single Circular Air-Hole Unit,” IEEE Photonics J. **8**(6), 1–11 (2016).
91. M. S. Islam, J. Sultana, A. Dinovitser, B. W. H. Ng, and D. Abbott, “A novel Zeonex based oligoporous-core photonic crystal fiber for polarization preserving terahertz applications,” Opt. Commun. **413**, 242–248 (2018).
92. M. S. Islam, J. Sultana, A. Dinovitser, M. Faisal, M. R. Islam, B. W. Ng, and D. Abbott, “Zeonex-based asymmetrical terahertz photonic crystal fiber for multichannel communication and polarization maintaining applications,” Appl. Opt. **57**(4), 666–672 (2018).
93. Z. Wu, X. Zhou, H. Xia, Z. Shi, J. Huang, X. Jiang, and W. Wu, “Low-loss polarization-maintaining THz photonic crystal fiber with a triple-hole core,” Appl. Opt. **56**(8), 2288–2293 (2017).
94. M. Cho, J. Kim, H. Park, Y. Han, K. Moon, E. Jung, and H. Han, “Highly birefringent terahertz polarization maintaining plastic photonic crystal fibers,” Opt. Express **16**(1), 7–12 (2008).

95. S. Atakaramians, S. Afshar V, B. M. Fischer, D. Abbott, and T. M. Monro, "Low loss, low dispersion and highly birefringent terahertz porous fibers," Opt. Commun. **282**(1), 36–38 (2009).
96. H. Chen, D. Chen, and Z. Hong, "Squeezed lattice elliptical-hole terahertz fiber with high birefringence," Appl. Opt. **48**(20), 3943–3947 (2009).
97. N. N. Chen, J. Liang, and L. Y. Ren, "High-birefringence, low-loss porous fiber for single-mode terahertz-wave guidance," Appl. Opt. **52**(21), 5297–5302 (2013).
98. D. Chen and H. Y. Tam, "Highly Birefringent Terahertz Fibers Based on Super-Cell Structure," J. Lightwave Technol. **28**(12), 1858–1863 (2010).
99. D. Chen and H. Chen, "Highly Birefringent Low-Loss Terahertz Waveguide: Elliptical Polymer Tube," J. Electromagnetic Waves and Applications **24**(11-12), 1553–1562 (2010).
100. D. Chen, "Mode Property of Terahertz Polymer Tube," J. Lightwave Technol. **28**(18), 2708–2713 (2010).
101. J.-L. Wang, J.-Q. Yao, H.-M. Chen, and Z.-Y. Li, "A Simple Birefringent Terahertz Waveguide Based on Polymer Elliptical Tube," Chin. Phys. Lett. **28**(1), 014207 (2011).
102. S. Yan, S. Lou, X. Wang, T. Zhao, and W. Zhang, "High-birefringence hollow-core anti-resonant THz fiber," Opt. Quantum Electron. **50**(3), 162 (2018).
103. H. Xiao, H. Li, B. Wu, Y. Dong, S. Xiao, and S. Jian, "Low-loss polarization-maintaining hollow-core anti-resonant terahertz fiber," J. Opt. **21**(8), 085708 (2019).
104. M. A. Mollah, S. Rana, and H. Subbaraman, "Polarization filter realization using low-loss hollow-core anti-resonant fiber in THz regime," Results Phys. **17**, 103092 (2020).
105. I. M. Ankan, M. A. Mollah, A. K. Paul, and K. Chakrabarti, "Polarization-maintaining and polarization-filtering negative curvature hollow core fiber in THz regime," in *2020 IEEE Region 10 Symposium (TENSYMP)* (IEEE, 2020), 612–615.
106. S. Yang, X. Sheng, G. Zhao, and S. Li, "Simple birefringent Terahertz fiber based on elliptical hollow core," Opt. Fiber Technol. **53**, 102064 (2019).
107. X. Tang, Y. Jiang, B. Sun, J. Chen, X. Zhu, P. Zhou, D. Wu, and Y. Shi, "Elliptical Hollow Fiber With Inner Silver Coating for Linearly Polarized Terahertz Transmission," IEEE Photonics Technol. Lett. **25**(4), 331–334 (2013).
108. H. Li, H. Xiao, J. Yuan, W. Wang, B. Yin, B. Wu, and Z. Han, "Terahertz polarization-maintaining subwavelength dielectric waveguides," J. Opt. **20**(12), 125602 (2018).
109. Y.-F. Zhu, X. Huang, Q. Ke, G. Liu, C.-F. Rao, D. Kong, S. Mei, Y. Liu, and H. Wang, "Low loss and polarization-insensitive coupling length for a terahertz fiber directional coupler with symmetric dual-suspended core structure," Opt. Commun. **480**, 126497 (2021).
110. B. Wang, F. Tian, G. Liu, R. Bai, L. Li, X. Yang, and J. Zhang, "A dual-core fiber for tunable polarization splitters in the terahertz regime," Opt. Commun. **480**, 126463 (2021).
111. M. Li and Y. Yang, "Single-and Multiple-Material Additively Manufactured Electronics: A Further Step From the Microwave-to-Terahertz Regimes," IEEE Microwave Mag. **24**(1), 30–45 (2023).
112. A. L. CruzI, V. Serrao, C. L. Barbosa, M. A. Franco, C. M. Cordeiro, A. A. Argyros, and X. J. J. O. M. Tang, Optoelectronics, and E. Applications, "3D printed hollow core fiber with negative curvature for terahertz applications," J. Microwaves Optoelectron. Electromagnet. Appl. **14**(1), 45–53 (2015).
113. L. D. van Putten, J. Gorecki, E. Numkam Fokoua, V. Apostolopoulos, and F. Poletti, "3D-printed polymer antiresonant waveguides for short-reach terahertz applications," Appl. Opt. **57**(14), 3953–3958 (2018).
114. A. L. Cruz, A. Argyros, X. Tang, C. M. Cordeiro, and M. Franco, "3D-printed terahertz Bragg fiber," *2015 40th International Conference on Infrared, Millimeter, and Terahertz waves (IRMMW-THz)* 1–2 (2015).
115. S. Li, Z. Dai, Z. Wang, P. Qi, Q. Su, X. Gao, C. Gong, and W. Liu, "A 0.1 THz low-loss 3D printed hollow waveguide," Optik **176**, 611–616 (2019).
116. J. Sultana, M. S. Islam, C. M. B. Cordeiro, M. S. Habib, A. Dinovitser, M. Kaushik, B. W. H. Ng, H. Ebendorff-Heidepriem, and D. Abbott, "Hollow Core Inhibited Coupled Antiresonant Terahertz Fiber: A Numerical and Experimental Study," IEEE Trans. THz Sci. Technol. **11**(3), 245–260 (2021).
117. M. Skorobogatiy, *Nanostructured and Subwavelength Waveguides: Fundamentals and Applications* (John Wiley & Sons, 2012), pp. 33–37.
118. K. Okamoto, *Fundamentals of Optical Waveguides* (Academic Press, 2006).
119. G. P. Agrawal, *Lightwave Technology: Telecommunication Systems* (John Wiley & Sons, 2005).
120. S. Ramachandran, *Fiber Based Dispersion Compensation* (Springer Science & Business Media, 2007), Vol. 5.